Summer 7-31-2020

How Oxygen-Binding Affects Structural Evolution of Even-Sized Gold Anion Clusters. (Size Range 20 to 34)

David Brunken-Deibert
david.deibert@huskers.unl.edu

HOW O_2-BINDING AFFECT STRUCTURAL EVOLUTION OF EVEN-SIZED GOLD CLUSTERS Au_n^- (n = 20-34)

by

David Brunken-Deibert

A Thesis

Presented to the Faculty of

The Graduate College at the University of Nebraska

In Partial Fulfillment of Requirements

For the Degree of Master of Science

Major: Chemistry

Under the Supervision of Professor Xiao Cheng Zeng

Lincoln, Nebraska

July, 2020

HOW O_2-BINDING AFFECT STRUCTURAL EVOLUTION OF EVEN-SIZED GOLD CLUSTERS Au_n^- (n = 20-34)

David Brunken-Deibert, MS

University of Nebraska, 2020

Advisor: Xiao Cheng Zeng

We report a joint anion photoelectron spectroscopy (PES) and theoretical study to investigate the effect of O_2-binding on the mid-sized even-numbered gold clusters, Au_n^- (n = 20−34), a special size region of bare gold clusters that entail rich forms of structural evolution and transformation. Specifically, within this size range, bare Au_{20}^- is a highly-symmetric pyramidal cluster, bare Au_{21-25}^- are flat-planar or hollow-tubular clusters, bare Au_{26}^- is the smallest core-shell gold cluster, while bare Au_{34}^- is a magic-number/fluxional core-shell cluster with the high-symmetry tetrahedral Au_4 core. In light of the strong size-dependent structural evolution of bare gold clusters in the n = 20−34 size range, we focused especially on the chemical interplay between the O_2 binding and the structure of the host gold clusters. The global minima of the O_2-bound gold clusters $Au_nO_2^-$ are searched using the basin-hopping global optimization technique in conjugation with density functional theory calculations. Vertical detachment energies are computed for the low-lying isomers with the inclusion of spin−orbit effects for gold to generate simulated photoelectron spectra and to compare with the experimental PES spectra. Based on the global−minimum structures identified, a series of structural transitions, from the pyramidal to fused−planar to core-shell structures, are identified for the $Au_nO_2^-$ clusters, where the O_2 binding is found to be in either *superoxo* or *peroxo* fashion, depending on the size and shape of the host gold clusters.

CHAPTER 1 Introduction

Gold nanoparticles show remarkable capability of catalyzing a variety of industrially and environmentally important chemical reactions such as CO oxidation,[1] ethylene epoxidation,[2, 3] selective hydrogenation,[4] C-C bond formation[5] and water-gas shift reaction.[6] Many of these reactions involve activation of oxygen molecule as a key step which is particularly challenging because of high kinetic stability of molecular oxygen owing to its triplet ground state and strong oxygen-oxygen bond. Many efforts have been made to explore more efficient nanoscale catalysts for the activation of molecular oxygen.[7-21] Particularly, both experimental and theoretical studies have been devoted towards the use of gold nanoclusters for oxygen activation in the CO oxidation reaction.[22-24]

The binding of molecular oxygen on bare gold cluster anions can help in understanding its activation process. Kaldor[25, 26] and Whettan[27] performed experimental studies on adsorption of O_2 on a series of gold cluster anions. They observed that only even−sized clusters are reactive towards oxygen. This is because the even−sized cluster anions possess an open-shell electronic configuration which can lead to more charge transfer from Au_n^- to O_2. By observation of O-O vibrational structures, subsequent anion photoelectron spectroscopy (PES) studies have shown that the molecular oxygen is chemisorbed on the Au_n^- clusters.[28, 29] Another PES study confirmed the molecular chemisorption and physisorption of O_2 on small-sized anionic gold clusters with even and odd number of atoms, respectively.[30] Among the even-sized clusters, Au_{10} and Au_{16} showed unusual behavior with Au_{16}^- being unreactive and Au_{10}^- being significantly less reactive towards molecular oxygen.[27] The chemical inertness of Au_{16}^- is due to its unique hollow-cage type structure and high electron binding energy.[31] The global-minimum structure of Au_{10}^- which possesses D_{3h} structure is unreactive towards O_2 while its other low-lying isomers are reactive.[32] Using infrared multiple photon dissociation spectra of $Au_nO_2^-$ clusters, Woodham et al.[33] have provided direct experimental evidence for O_2 adsorption in *superoxo* mode (binding through one oxygen atom). Previously, while studying O_2 adsorption on even-sized gold clusters in the range of $n = 2-20$, we have revealed a *superoxo* to *peroxo* (binding through both the oxygen atoms) binding transition of O_2 molecule on anionic gold clusters occurs at Au_8^-.[34] Specifically, it was observed that $n = 2, 4, 6$ involve superoxo binding and $n = 10, 12, 14, 18$ involve peroxo binding, whereas a re-emergence of superoxo binding occurs at $n = 20$ due to the high-symmetry tetrahedral structure of Au_{20}^{-}, which has a very low electron affinity. O_2-deirved low binding energy features were observed in the experimental spectrum of $Au_nO_2^{-}$ (n = 2, 4, 6, 8 and 20). Note that no direct comparison of the experimental and theoretical PE spectra was presented for $Au_{20}O_2^{-}$ at that time. Hence, the superoxo O_2 binding site on the pyramidal Au_{20}^{-} cluster and possible presence of any minor isomer contributors towards the experimental PES spectrum were not reported.

Apart from the experimental studies, several computational studies have also been performed to investigate O_2 binding on bare gold clusters.[35-44] Mills *et al.*[39] reported that O_2 binds more strongly with neutral and anionic gold clusters having odd number of electrons. Yoon *et al.*[36] found that small-sized anionic gold clusters (n = 1−3) favor molecular adsorption and large-sized clusters (n = 4−8) favor dissociative adsorption. It was also reported that O_2 dissociation requires very high activation energy. The high activation barriers are consistent with the experimental observation of only chemisorbed O_2 species on the even−sized Au_n^{-} clusters for $n \leq 20$[25, 27-29, 45] as well as physisorbed odd−sized Au_n^{-} for n = 3, 5, 7.[30] Several other computational studies have been carried out to examine the effect of charge state,[46-48] doping,[49-52] co-adsorption,[4, 53] and substrate support,[52, 54-56] on the O_2 interactions with gold clusters.

Thus far, the experimental O_2 binding studies have mostly been focused on small-sized gold clusters. To our knowledge, there have been no joint experimental and theoretical studies which investigate the effect of O_2 binding on the structural transitions in mid−sized gold clusters. In this work, we report a combined experimental anion PES and theoretical study of O_2 binding on even−sized Au_n^{-} clusters (n = 20−34). We have particularly chosen these mid−sized range of gold clusters because they belong to a special size region where rich structural evolution and transition occurs as well as several distinct structures coexist for each size.[57, 58] Apart from the O_2 binding mode, we are particularly interested in how the O_2 bind affect the structural evolution in the gold cluster anions. Interestingly, we observe a core-shell type structure for $Au_nO_2^{-}$ at n = 24. In fact, this is the smallest $Au_nO_2^{-}$ cluster with a gold core. In their bare Au_n^{-} counterparts, the smallest core-shell gold cluster is Au_{26}^{-}.[59]

Please note that this work is a joint experimental/theoretical study. The experimental measurement was performed by Professor Lai-Sheng Wang group at Brown University. The theoretical calculations have been divided into several tasks: (1), (2), (3) … (11). Tasks (1), (5), and (7) were performed and/or initiated by Dr. Navneet Singh Khetrapal and finished by me, whereas tasks (2), (3), (4), (6), (8), (10) and (11) were completed by me. Task (9) were both independently carried out by Dr. Khetrapal and me to verify assignments.

Task (1) consisted of Basin-Hopping-DFT calculations for isomers *n*=20-24, 34. Task (2) consisted of optimizing generated isomers using the fine integration grid at both doublet and quartet multiplicities. Task (3) consisted of Basing-Hopping DFT calculations for Au_n^- isomers where *n*=26-32. Task (4) was the same as Task (2) with isomers *n*=26-32 range. Task (5) involved the re-optimization of isomers *n*=20-24,34 using the PBE0 functional with the CRENBL-ECP basis set using Gaussian 16. Task (6) used the PBE0 functional with the TZP basis set using ADF2013 software package for isomers where *n*=26-32. Task (7) performed the single point energy calculations using PBE0/CRENBL-ECP using NWChem 6.6 for isomers *n*=20-24,34, Task (8) was identical as Task (7) except using isomers *n*=26-32. During Task (9) all produced theoretical spectra were compared to experimental spectra when available. After assignments were made Task (10) involved using the basis set superposition error calculations to determine adsorption energy of assigned isomers. Task (11) calculated the Bader Charge distribution of the assigned isomers.

CHAPTER 2 Experimental Methods

The experiment was carried out by Professor Lai-Sheng Wang group at Brown University using a magnetic-bottle PES apparatus equipped with a laser vaporization cluster source, details of which have been published elsewhere.[60-62] Here, a brief description of the experimental methods is given: A gold disk target was vaporized by a pulsed laser to generate a plasma inside a large-waiting-room cluster nozzle. A high-pressure helium carrier gas pulse was delivered to the nozzle at the same time, cooling the plasma and initiating nucleation. For the O_2 binding experiment, we used a helium carrier gas seeded with 0.1% O_2, which reacts with the gold clusters inside the nozzle to form various $Au_nO_2^-$ complexes. Clusters formed inside the nozzle were entrained in the helium carrier gas and then underwent a supersonic expansion. After a skimmer, anions from the collimated cluster beam were extracted at 90° into a time-of-flight mass spectrometer. Clusters of interest were selected by a mass gate and decelerated before being photo-detached by a 193 nm laser beam from an ArF excimer laser. Photoelectrons were collected by a magnetic bottle at nearly 100% efficiency into a 3.5 m long electron flight tube for kinetic energy analyses. The photoelectron kinetic energies were calibrated by the known spectra of Au^- and subtracted from the photon energies to attain the reported electron binding energy spectra. The electron kinetic energy resolution of the apparatus is $\Delta E_k / E_k$ ~2.5%, that is, approximately 25 meV for 1 eV electrons.

CHAPTER 3 Computational Methods

The Basin-Hopping (BH) global optimization method[63, 64] in conjugation with density-functional theory (DFT) optimization was employed for the search of global−minimum structures of $Au_nO_2^-$. After each accepted Monte Carlo move during the BH search, the resulting local-minimum geometry was re-optimized with Perdew−Burke−Ernzerhof (PBE) exchange−correlation functional[65] and the double-numerical polarized (DNP) basis set with effective core potential (ECP), implemented in the DMOL^3 4.0 program.[66, 67] Loose integration grid was used for the DFT calculations at this step. Both biased and unbiased BH searches were performed. In the biased search, the coordinates of the two oxygen atoms were fixed and all the gold atoms could relax. In the unbiased BH search, all oxygen and gold atoms could move. More than 1000 unique isomers were collected for each cluster size. This isomer population consisting of the structures with both molecularly chemisorbed oxygen (O_2 binding) as well as dissociated oxygen (atomic O binding). Extensive studies have shown that although dissociated oxygen isomers are generally the global minimum, the high energy barrier for O_2 dissociation cannot be overcome under the experimental PES conditions.[32] Therefore, the top 40−60 isomers with only molecularly adsorbed oxygen obtained from the BH global optimization were considered as the candidates for the lowest-lying structures. These isomers were optimized again using DMOL^3 4.0 program using the fine integration grid. Both doublet and quartet multiplicities were considered at this step.

Next, the candidate isomers with the lower energy spin multiplicity were re-optimized using the PBE0 functional[68] with the CRENBL−ECP[69] basis set implemented in the Gaussian16 package.[70] The CRENBL-ECP uses sixty core electrons for the effective core potential of gold and two core electrons for oxygen. However, for candidate isomers in n= 26−32 range, the re−optimization was performed at the PBE0/TZP level of theory functional with inclusion of the relativistic effects under zeroth-order regular approximation (ZORA) as implemented in the

ADF2013 software package.[71-73] During this re−optimization step, some of the structures were found to converge to the same geometry. This reduced the number of candidate isomers for each cluster size. Lastly, single-point energy computations of the reoptimized geometries were performed using the PBE0 functional with CRENBL−ECP basis set and with inclusion of the spin−orbit (SO) effects for the gold atoms, all implemented in the NWCHEM 6.6 package.[74] The inclusion of SO effects for gold has been proven to result in quantitative or nearly quantitative agreement between the experimental and simulated PES spectra for bare gold, gold−alloy, as wells as CO-bound gold anion clusters.[57, 75-79] The first vertical detachment energy (VDE) was calculated as the energy difference between the neutral and anion at the PBE0 optimized anion geometry. The binding energies of deeper occupied orbitals were added to the first VDE to generate electronic density of states. Each VDE was fitted with a gaussian of 0.035 eV width to yield simulated PES spectra, which were compared with the experimental PES spectra to identify the structures that give the best agreement between the simulation and measurement. The energy gap (eV) between the first and second highest occupied molecular orbitals, representing the gap between peaks labeled X and A was also calculated for all the candidate isomers.

CHAPTER 4 Results and Discussion

The experimental PES spectra of $Au_nO_2^-$ (n = 20, 22, 24 and 34) at 193 nm (6.424 eV) photon energy and their comparison with the simulated photoelectron spectra of the low-lying (both major and minor) isomers are shown in Figures 1-4, respectively. The observed features are labeled by capital letters X, A, B, C,..., where X denotes the transition from the ground state of the anion to that of the neutral, and A, B, C, ... denote detachment transitions to the excited states of the neutral cluster. Weaker features labeled with X′, A′ ... indicate they are from minor isomers. Also, in some figures, the weak features are labeled with *, representing the presence of unidentified minor isomers. For the sake of discussion, the 193 nm experimental PES spectra along with the simulated spectra of assigned structures of bare gold clusters, Au_n^- (n = 20, 22, 24 and 34) from a previous studies[57, 58, 80, 81] are also presented in Figures 1-4.

The experimental first VDEs and the energy gap (energy difference between peaks labeled X and A) are given in Table 1, along with the computed first VDEs and relative energies calculated at the PBE0/CRENBL-ECP (with and without the inclusion of SO effects for gold) level of theory for the top candidates. A systematic decrease in the binding energy is present in theoretical VDEs with respect to the experimental ones due to the SO coupling used for the theoretical calculations. Therefore, it is unreasonable to directly compare the VDE values obtained from the experimental and theoretical PES spectra. Instead, we have used root-mean-square deviation (RMSD) and X-A energy gaps as quantitative tools for comparison of the simulated spectra with the experimental ones. The first peak of the simulated spectra was aligned with the first experimental VDE (X) and then the RMSD was calculated for the subsequent peaks of the simulated spectra with respect to the corresponding experimental peaks. The theoretical energy gaps show excellent agreement with the experimental values with an average deviation of 0.033 eV. The RMSD and the X-A values (of the major/singly assigned isomers highlighted in bold) given in Table 1 confirm that the selected level of theory is appropriate for the $Au_nO_2^-$ species in the current study. In our previous studies, we have successfully used a combination of visual inspection, relative energy comparison, and RMSD in peak positions for the identification of global-minimum structures of gold clusters and CO-bound gold clusters.[75-77, 79] For each cluster size, the structures are named with roman numerals (I, II, III….) which are based on the order of increasing energies at PBE0/CRENBL-ECP level of theory. Hereafter, the PBE0/CRENBL-ECP and PBE0/CRENBL-ECP//PBE0/CRENBL-ECP (with SO effects for Au) levels of theory are referred to as PBE0 and SO-PBE0, respectively.

Table 1. Experimental first VDE labeled as X in Figures 1-4, the energy gap between peaks labeled X and A from the 193 nm PE spectra for $Au_nO_2^-$ (n = 20–34), relative energies computed at PBE0/CRENBL-ECP (ΔE_a) and PBE0/CRENBL-ECP (with SO effects for Au) (ΔE_b) levels (with all isomers being optimized at the PBE0/CRENBL-ECP level), theoretical first VDE, energy gaps (X-A) and root-mean-square deviation (RMSD) in the theoretical peak positions with respect to the experimental peak positions. All energies are in eV. The X-A gaps of the major/singly assigned isomers are highlighted in bold.

Anion Cluster	Experimental[a]		Theoretical					
	VDE	X-A Gap	Isomer	ΔE_a	ΔE_b	VDE	X-A Gap	RMSD
$Au_{20}O_2^-$	3.81 (X') 3.62 (X)	0.54	VII	0.000	0.000	4.08	0.14 (X'-A)	0.044
			XIV	0.263	0.253	3.47	**0.51**	0.023
			XIX	0.335	0.333	3.78	0.16	0.062
$Au_{22}O_2^-$	3.65 (X) 3.49 (X')	0.45	IV	0.098	0.387	3.53	**0.50**	0.0022
			XXIII	0.505	0.835	3.34	0.61 (X-A')	0.0037
$Au_{24}O_2^-$	3.44 (X)	0.40	XII	0.227	0.511	3.35	**0.40**	0.67
$Au_{34}O_2^-$	4.37 (X) 3.93 (X') 4.11 (X")	0.10	I	0.000	0.000	4.20	**0.15**	0.0049
			XII	0.539	0.535	3.84	0.53 (X'-A')	0.0015
			XVI	0.577	0.573	4.00	0.37 (X"-A")	-

[a] Experimental uncertainty: ±0.01 eV.

$Au_{20}O_2^-$

The 193 nm spectrum (Figure 1a) of $Au_{20}O_2^-$ exhibits broad weak peaks. Seven major peaks (X, A-F) were identified, as well as one minor peak. The initial band, designated X', at 3.62 eV denotes the region where an anion cluster transitions to that of the neutral state. The smaller band, X at 3.81 eV, represents the contribution from another isomer. These two weak bands are attributed to the unresolved O-O vibrational progressions due to photodetachment of a superoxo unit.[29, 30, 34] Subsequent regions, labeled A-F respectively, represent excited state transitions of the neutral cluster. They can be found at 4.16, 4.35, 4.58, 4.78, 4.96, and 5.24 eV.

A total of 22 low-lying isomers were examined, out of which the simulated spectra of three candidate isomers are compared with that of the 193 nm experimental PES spectrum in Figures 1c-e. A combination of three isomers (with isomer XIV as the major, isomers VII and XIX as the minor contributors towards the experimental PES spectrum) is found to accurately replicate the experimental spectrum. The RMSD between the peaks of the experimental spectrum and the peaks of the combined spectrum of the assigned isomers is calculated to be 0.061. The major isomer XIV shows superoxo O_2 binding with the gold nanocluster. The two minor isomers exhibit peroxo O_2 binding. In all the three structures, the stable tetrahedral pyramidal Au_{20}^- motif is present.[34,61] Energetically, isomer VII is the lowest in energy at both PBE0 and SO-PBE0 levels. While the isomers XIV and XIX are higher in energy. Isomer XIV has a relative energy of 0.263 eV and 0.253 eV at PBE0 and SO-PBE0 levels, respectively. Isomer XIX is even higher in energy with relative energy of 0.335 eV and 0.333 eV at PBE0 and SO-PBE0 levels, respectively.

In the major isomer XIV, the oxygen is adsorbed in superoxo mode on an apex site of the Au_{20} pyramid. Its simulated PES spectrum has twelve bands within the experimental window at 3.78, 3.94, 4.09, 4.43, 4.55, 4.81, 5.29, 5.45, 5.52, 5.77, 5.85, and 5.96 eV. Out of the twelve bands three bands are found to contribute significantly to the experimental spectrum. The band with peak at 3.78 eV describes experimental peak X, the band at 4.43 eV reproduces experimental peak C, and the peak at 4.81 eV reproduces peak E.

The minor isomer VII has the oxygen adsorbed in a peroxo fashion on one of the apex sites of its pyramidal structure. Like isomer XIV, its PES spectrum also demonstrates twelve peaks within the experimental range. Three peaks at 3.47, 3.97, and 5.14 eV reproduce the experimental peaks X', A, and F, respectively of the experimental spectrum.

The minor isomer XIX has the oxygen adsorbed on the lateral edge of the pyramidal cluster in a peroxo fashion. In the simulated PES spectrum, again there are twelve peaks within the experimental range. Band peaks are found at 4.08, 4.22, 4.33, 4.51, 4.57, 4.83, 4.89, 5.20, 5.50, 5.69, 5.84, and 5.97 eV. Two of these peaks, 4.22 and 4.57 eV, reproduce two experimental peaks for bands B and D within the experimental spectrum.

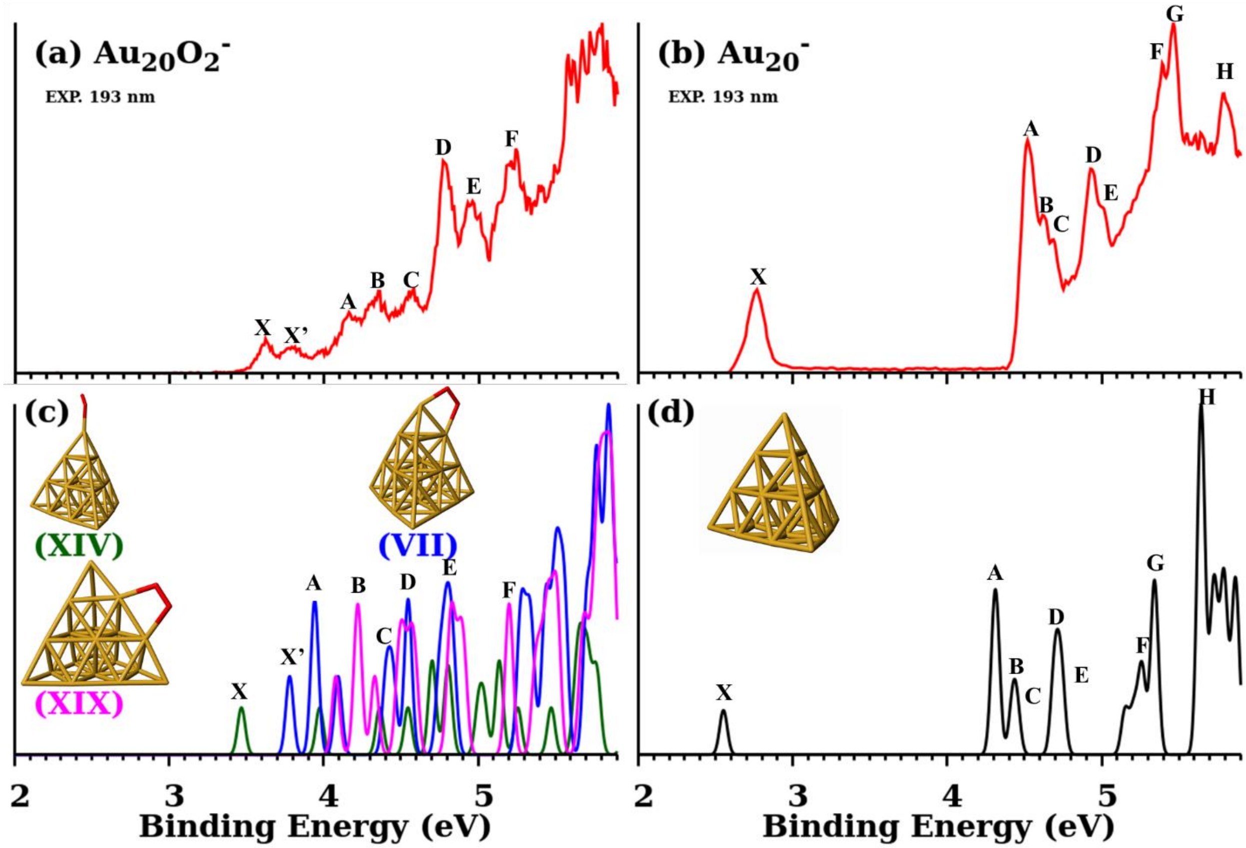

Figure 1. Comparison of the simulated spectra (lower panels) with the 193 nm experimental spectra (upper panels) for the low-lying isomers of $Au_{20}O_2^-$ and bare Au_{20}^- (see Ref. 80). The oxygen molecule is in red.

$Au_{22}O_2^-$

The 193 nm spectrum of $Au_{22}O_2^-$ (Figure 2a) shows broad weak peaks. However, sharp well-defined peaks are also present at higher binding energies. This suggests that there are superoxo and peroxo isomers coexisting. There exist two weak initial peaks corresponding to individual ground states of the two coexisting isomers. The major isomer band at ~3.65 eV denoted X and the minor isomer X' at ~3.49 eV. Subsequent bands are denoted A, B, C, D, E, and F, located at 4.10, 4.35, 4.46, 4.58, 4.71, and 4.89 eV, respectively. Remaining bands are too poorly resolved to meaningfully analyze.

A total of 30 low-lying isomers were examined. Two of these isomers (IV and XXIII) are found to reproduce the experimental PES spectrum (Figures 2c-d) . Although the major isomer IV possesses a lower degree of symmetry than that of the $Au_{20}O_2^-$ clusters, yet a deformed tetrahedral pyramidal motif is clearly visible in its case. The tetrahedral pyramidal motif is completely absent in case of the minor isomer XXIII which exhibits a flat-cage type structure with relatively higher degree of symmetry (C_2). The O_2 binding is in a peroxo fashion in case of the major isomer while a superoxo type binding on an apex site is observed in case of the minor isomer. The simulated PES spectrum of the major isomer can accurately reproduce six major peaks of the experimental spectrum: X, A, B, C, D and E at 3.34, 4.95, 4.21, 4.46, 4.59, and 4.78 eV, respectively. The minor isomer can account for the weak band X' (3.49 eV). This feature is resulted from the O−O vibrational excitation upon photodetachment from the minor isomer.[29, 30, 34] The bands B', C', D', E', and F' of the minor isomer are buried under those of the major isomer in the combined PES spectrum. The RMSD between the peaks of the experimental spectrum and the peaks of the combined spectrum of the assigned isomers is calculated to be 0.037. Isomer IV has a relative energy of 0.098 eV and 0.387 eV at PBE0 and SO-PBE0 levels, respectively. While the minor isomer XXIII has a relative energy of 0.505 eV and 0.835 eV at PBE0 and SO-PBE0 levels, respectively.

The minor isomer XXIII has a striking resemblance to one of the assigned the bare isomers (isomer III) of Au_{22}^-. The structures are nearly identical except for a displaced gold atom. The major isomer IV on the other hand, is very different from the assigned bare clusters as the tetrahedral pyramidal motif is absent in case of the bare Au_{22}^- isomers. It seems that the O_2 binding has a much greater effect on the structure of Au_{22}^- cluster than in the case of the magic-number and high-symmetry Au_{20}^- cluster.

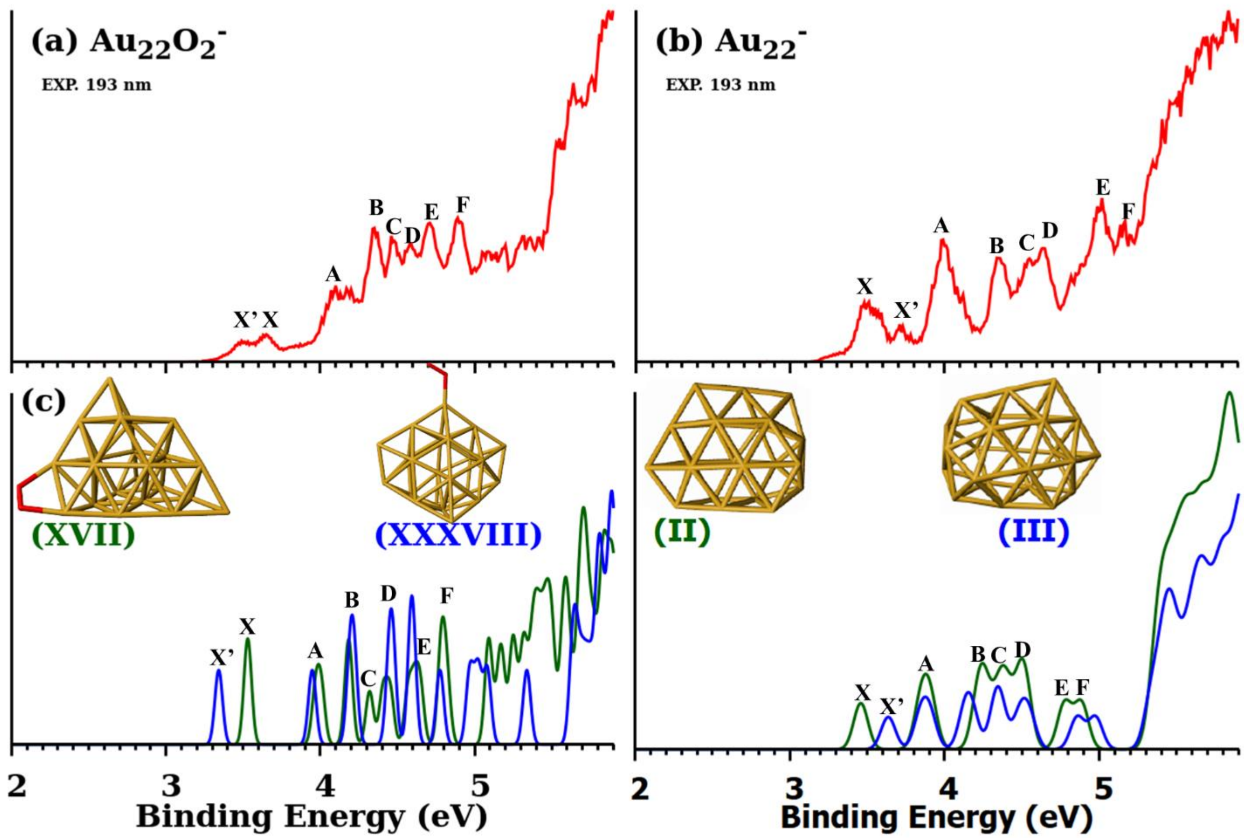

Figure 2. Comparison of the simulated spectra (lower panels) with the 193 nm experimental spectra (upper panels) for the low-lying isomers of $Au_{22}O_2^-$ and bare Au_{22}^- (see Ref. 57). The oxygen molecule is in red.

$Au_{24}O_2^-$

The experimental PES spectrum (Figure 3a) showed seven clear peaks at 3.44, 3.84, 4.16, 4.58, 4.92, 5.11, 5.21, and 5.38 eV. Following the naming scheme outlined earlier, the first peak was designated X, while subsequent peaks were labeled A-G, respectively. The sharper nature of the bands than those of $Au_{20}O_2^-$ and $Au_{22}O_2^-$ and the absence of weak features in low-binding region indicate that the O_2 binding is in peroxo mode.

Out of the 35 examined low-lying isomers, isomer XII (Figure 3c), can accurately reproduce the experimental PES spectrum. The initial X band is observed at 3.35 eV, and the bands A-G are observed at 3.76, 4.03, 4.48, 4.78, 4.87, 5.13, and 5.34 eV, respectively. After accounting for the 0.09 eV red shift, the calculated RMSD between the experimental and theoretical spectrum was 0.067. Isomer XII as predicted has O_2 binding in a peroxo mode. Unlike the bare Au_{24}^-

clusters where hollow-tubular structure is dominant,[57, 58] the $Au_{24}O_2^-$ exhibit a core-shell with one atom core. This illustrates that upon O_2 binding the structure of Au_{24}^- cluster changes significantly. This is the smallest reported O_2-bound gold cluster with a core atom. Energetically, Isomer XII has a relative energy of 0.227 eV and 0.511 eV at PBE0 and SO-PBE0 levels, respectively.

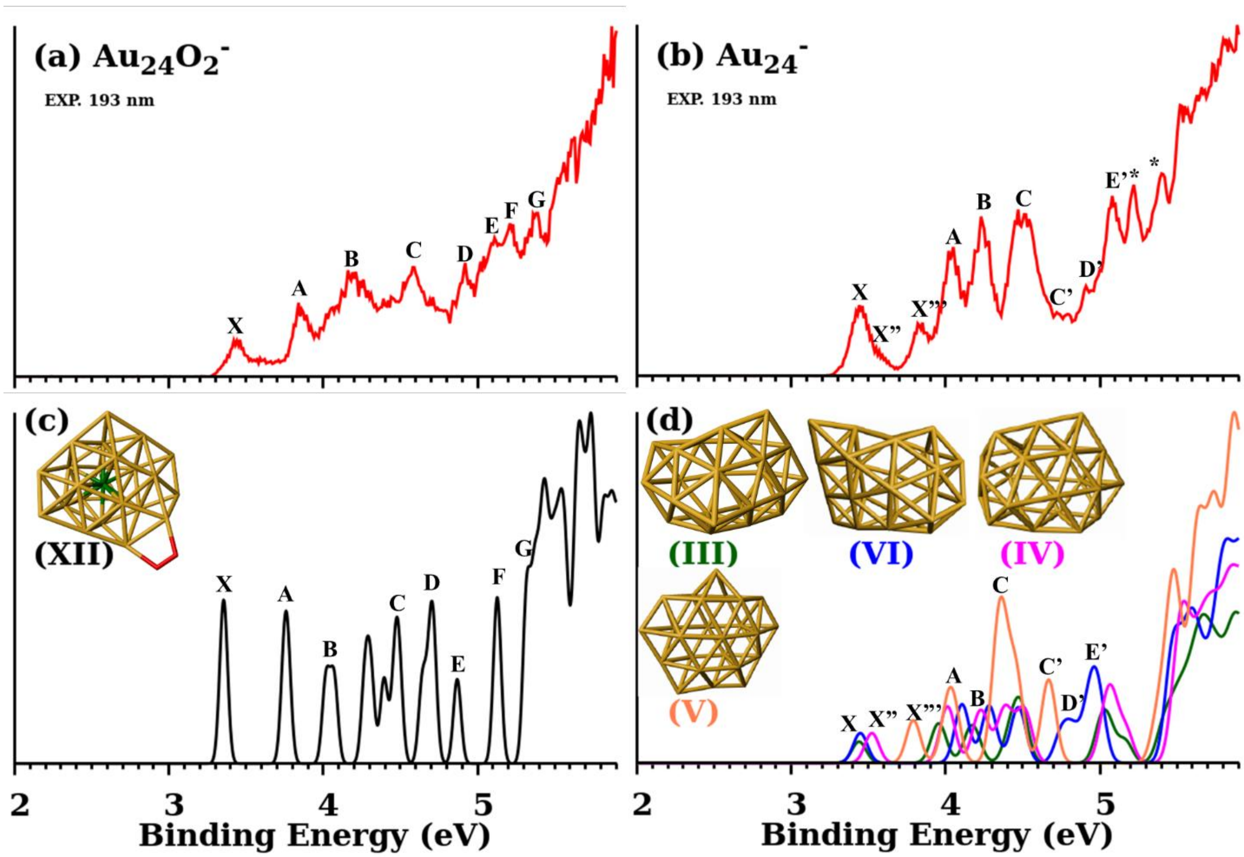

Figure 3. Comparison of the simulated spectra (lower panels) with the 193 nm experimental spectra (upper panels) for the low-lying isomers of $Au_{24}O_2^-$ and bare Au_{24}^- (see Ref. 57). The gold atom in green denotes the atom in the core of the cluster. The oxygen molecule is in red.

$Au_nO_2^-$ (n = 26−32)

Currently, the experimental PES spectra for the clusters in this range are not available. The simulated spectra for each cluster size in this range and their corresponding relative energies, VDE and X-A gap data is presented in Figures 7-10 and Tables 2-5, respectively. For now, we tentatively assign the lowest-energy isomers for each cluster size as the global minima. Definite assignments can be made in future when the experimental data is available. The structures of the assigned isomers are presented in Figure 6.

$Au_{34}O_2^-$

The experimental PES spectrum of $Au_{34}O_2^-$ consists of weak bands in the low binding energy region. Followed by the bands with relatively higher intensity and a high degree of overlap. The unique character and high degree of overlap made the determination of the global minimum structure especially difficult. Seven major peaks A-G are observed at 4.37, 4.47, 4.51, 4.68, 4.82, 5.02, 5.25, and 5.41 eV. Then two minor peaks being labeled X' at 3.93 eV and X'' 4.14 eV, respectively. These two features are likely due to the O−O vibrational excitation upon photodetachment of O_2 binding in superoxo mode.[29, 30, 34] There is a small unresolved peak, designated *, at approximately 3.42 eV. The experimental spectrum shows a strong similarity to that of the bare Au_{34}^- cluster. This indicates that the Au_{34}^- structure changes little upon the O_2 binding.

We examined 55 low-lying isomers; out of which isomer I (Figure 4c-d) accurately reproduces the major bands of the experimental PES spectrum. Its simulated PES spectrum can reproduce the bands X, A-G at 4.21, 4.33, 4.37, 4.52, 4.68. 4.86, 5.10, and 5.27 eV, respectively. The two minor bands X' and X" in the low binding energy region can be assigned to the isomers XII and XVI, respectively. These isomers are the minor contributors towards the experimental PES spectrum. A red shift of about 0.088 eV is observed in the theoretical peaks and the RMSD is calculated to be 0.058. Overall, a constructive combination of the simulated spectra of three isomers is in good agreement with the experimental spectrum. Isomer I is the lowest in energy at both PBE0 and SO-PBE0 levels. While isomer XII has a relative energy of 0.539 eV and 0.535 eV at PBE0 and SO-PBE0 levels, respectively. Isomer XVI has a relative energy of 0.577 eV and 0.573 eV at PBE0 and SO-PBE0 levels, respectively. In case of isomer I, the oxygen molecule is chemisorbed in the peroxo style. Whereas the two minor isomers exhibited superoxo type O_2 binding. The superoxo adsorption observed in the minor isomers is supported by the fact that both X' and X" are very board peaks. The major as well as two minor isomers contain a tetrahedral Au_4 core, the same as the one observed in case of the bare Au_{34} cluster.[81] The structures of the isomer I and the bare Au_{34}^- are very similar. This is confirmed by very small RMSD of 1.18 Å in the atomic positions of gold atoms between the two structures.

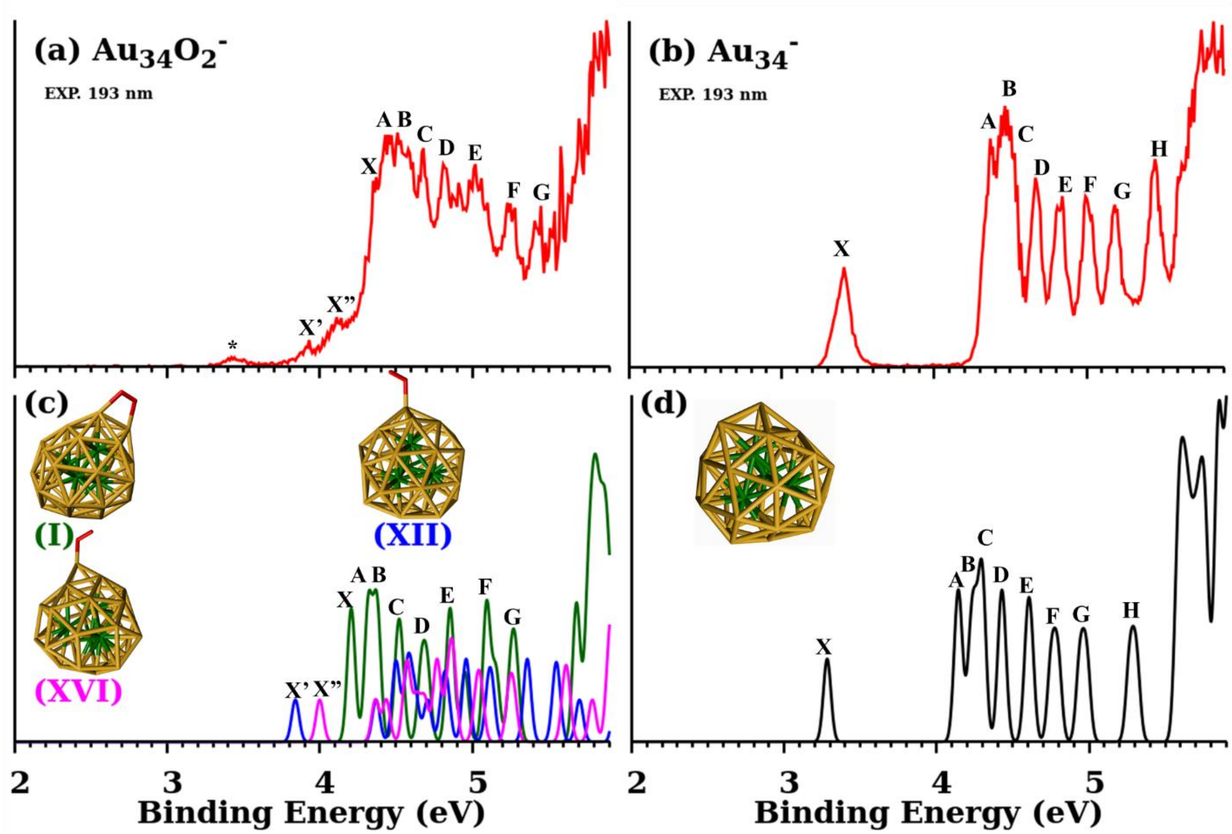

Figure 4. Comparison of the simulated spectra (lower panels) with the 193 nm experimental spectra (upper panels) for the low-lying isomers of $Au_{34}O_2^-$ and bare Au_{34}^- (see Ref. 81). The gold atoms in green denote the atoms in the core of the cluster. The oxygen molecule is in red.

Adsorption Energies and Bader charges

The adsorption energies of O_2 on the Au_n^- clusters is calculated as follows:

$$\Delta E_{ads} = E_{ZPE,\ BSSE}(Au_nO_2^-) - E_{ZPE}(Au_n^-) - E_{ZPE}(O_2),$$

where E represents the electronic energy. The subscript ZPE represents that the electronic energy includes with the zero-point energy correction. For gold-cluster-O_2 ($Au_nO_2^-$) complexes, the basis set superposition error (BSSE) was taken into the account in which gold cluster Au_n^- and O_2 were treated as two separate fragments. A more negative value of ΔE_{ads} reflects more favorable adsorption. The change in the calculated ΔE_{ads} with respect to number of gold atoms *n* are shown in Figures 5a. In case where more than one isomer is assigned, the ΔE_{ads} is only shown for the major isomer. As expected, $Au_nO_2^-$ complexes which show superoxo O_2 binding have a lower

ΔE_{ads} than the ones which exhibit peroxo type O_2 binding. Among the five clusters, $Au_{30}O_2^-$ shows the most favorable O_2 binding while $Au_{26}O_2^-$ shows the least favorable adsorption.

To understand the charge transfer upon the O_2 binding, we perform the Bader charge analysis[82-84] of the $Au_nO_2^-$ clusters. The Bader charges (B_c) of the Au_n^- and O_2 fragments of the $Au_nO_2^-$ cluster are presented in Figure 5b. A charge transfer of about 0.6e from Au_n^- to O_2 is observed in all the cases except $Au_{32}O_2^-$ where only a 0.12e of charge is transferred. This is because a quartet spin multiplicity is more stable in case $Au_{32}O_2^-$.

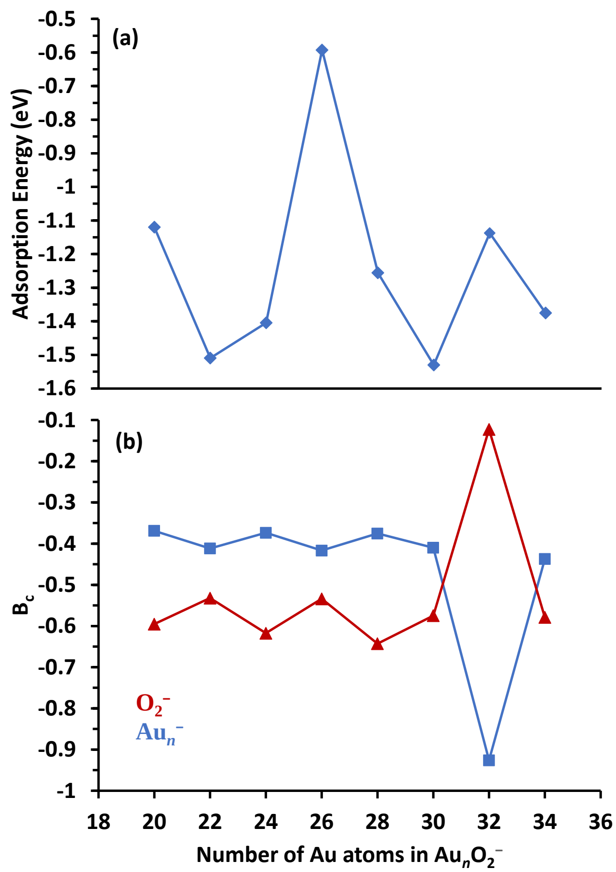

Figure 5. Size dependences of (a) O_2 adsorption energies (ΔE_{ads}) for the best candidate isomer of $Au_nO_2^-$ (n = 20-34) clusters identified and (b) change in Bader charges (B_c) for the host gold cluster Au_n^- and the adsorbed O_2^- for the best candidate isomer of $Au_nO_2^-$ (n = 20-34) clusters.

Structural Evolution of $Au_nO_2^-$ (n = 20−34) clusters with even numbered gold atoms

The identified most stable structures for the O_2-bound gold cluster anions are shown in Figure 6. This special size range of bare gold clusters is known for exhibiting a variety of distinct structures, including pyramidal, hollow-tubular, fused-planar and core-shell. For n = 20, the highly-symmetric pyramidal Au_{20} motif is observed in both major and minor isomers, with the O_2 binding in the superoxo fashion in the major isomer and a peroxo fashion in both the minor isomers. A distorted pyramidal Au_{20} motif (shown in blue) with an intact triangular Au_{10} face is observed again in the major isomer of $Au_{22}O_2^-$. The minor isomer at n = 22, has a fused-planar structure. The O_2 shows peroxo binding in the major isomer, while superoxo O_2 binding in the minor isomer at n = 22. A core-shell structure emerges at n = 24 with one core gold atom with the O_2 binding in peroxo fashion. Please note that Au_{24}^- is the smallest gold cluster anion which transforms to a core-shell type structure upon O_2 binding. The core-shell structures with core atom remain dominant in the n = 24−28 range with the O_2 binding in superoxo fashion at n = 26, and in peroxo fashion for n = 28 and 30. $Au_{32}O_2^-$ exhibits a triangular Au_3 core while the highly-symmetric tetrahedral Au_4 core is observed in the major as well as minor isomers of $Au_{34}O_2^-$. A superoxo O_2 binding is observed in case of $Au_{32}O_2^-$ while a peroxo O_2 binding is observed in case of the major isomer of $Au_{34}O_2^-$. Both the minor isomers of $Au_{34}O_2^-$ exhibit a superoxo O_2 binding.

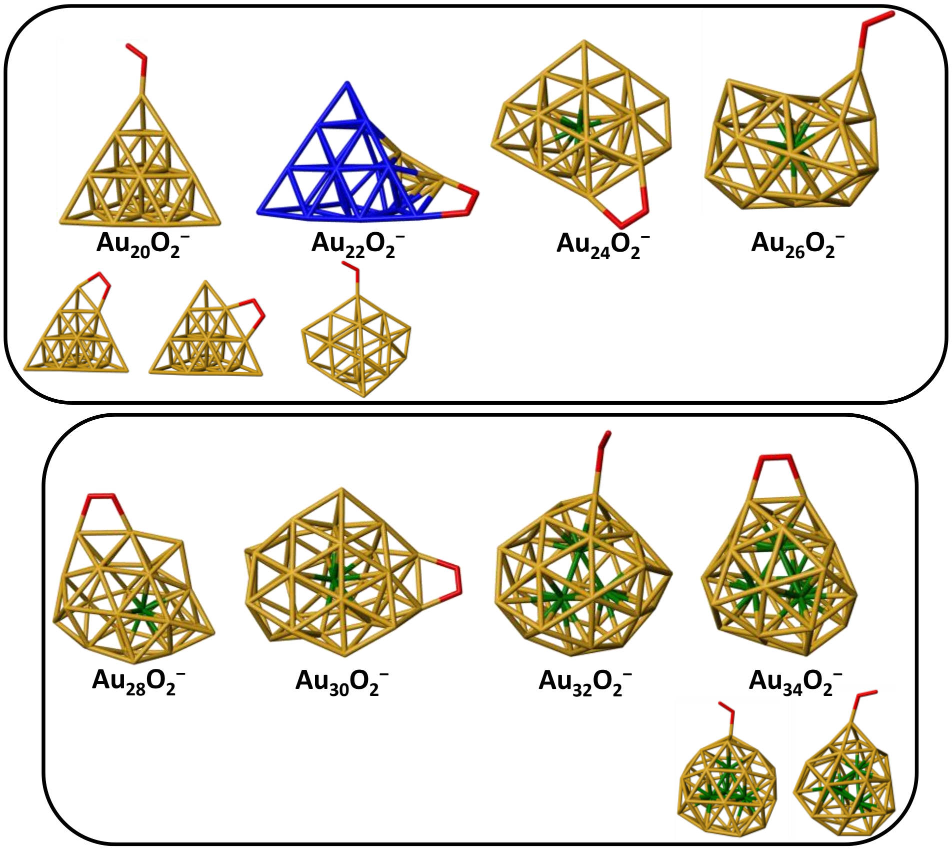

Figure 6. Structural evolution of the O_2 adsorbed even-numbered gold cluster anions $Au_nO_2^-$ *(n = 20 - 34)*. The size of the minor isomers is plotted smaller than that of the major isomers. The gold atoms in green denote the atoms in the core of the cluster. The oxygen molecule is in red. The original tetrahedral pyramidal face of $Au_{22}O_2^-$ is shown in blue.

CHAPTER 6 Conclusions

In summary, we report a joint theoretical and experimental photoelectron spectroscopy study of O_2 binding on medium-sized even-numbered gold anion clusters, Au_n^- (n = 20−34). Photoelectron spectra are measured for the clusters (n = 20−24, 34) and used to compare with theoretical calculations for the identification of the most stable structure in the cluster beam. The basin-hopping global-minimum search for this size range yielded diverse structures for the O_2-bound gold clusters, such as pyramidal, fused-planar, and core-shell. Transition from the pyramidal to fused-planar to core-shell structures for the host gold clusters Au_n^- and the O_2 binding in both superoxo and peroxo fashions are observed. Notably, the O_2-bound $Au_{24}O_2^-$ is the smallest cluster with a core-shell type structure for the gold. This is in stark contrast with the hollow-tubular type structures found dominant for the bare Au_{24}^- cluster. The n = 30 size of bare gold cluster is predicted to be the most favorable for the O_2 binding as this size exhibits the strongest binding ability.

Acknowledgements

The computational work is done by using computer facility in University of Nebraska Holland Computing Center.

References

1. Haruta, M., Size- and support-dependency in the catalysis of gold. *Catalysis Today* **1997,** *36*, 153-166.
2. Nijhuis, T. A.; Visser, T.; Weckhuysen, B. M., Mechanistic Study into the Direct Epoxidation of Propene over Gold/Titania Catalysts. *The Journal of Physical Chemistry B* **2005,** *109*, 19309-19319.
3. Sinha, A. K.; Seelan, S.; Akita, T.; Tsubota, S.; Haruta, M., Vapor phase propylene epoxidation over Au/Ti-MCM-41 catalysts prepared by different Ti incorporation modes. *Applied Catalysis A: General* **2003,** *240*, 243-252.
4. Juliusa, M.; Robertsa, S.; Fletchera, J. C. Q., A review of the use of gold catalysts in selective hydrogenation reactions Lynsey McEwana. *Gold Bulletin* **2010,** *43*, 298-306.
5. Tsunoyama, H.; Sakurai, H.; Ichikuni, N.; Negishi, Y.; Tsukuda, T., Colloidal Gold Nanoparticles as Catalyst for Carbon−Carbon Bond Formation: Application to Aerobic Homocoupling of Phenylboronic Acid in Water. *Langmuir* **2004,** *20*, 11293-11296.
6. Bond, G., Mechanisms of the gold-catalysed water-gas shift. *Gold Bulletin* **2009,** *42*, 337-342.
7. Oemry, F.; Nakanishi, H.; Kasai, H.; Maekawa, H.; Osumi, K.; Sato, K., Adsorbed oxygen-induced cluster reconstruction on core–shell Ni@Pt and Pt clusters. *Journal of Alloys and Compounds* **2014,** *594*, 93-101.
8. Dar, M. A.; Krishnamurty, S., Molecular and Dissociative Adsorption of Oxygen on Au–Pd Bimetallic Clusters: Role of Composition and Spin State of the Cluster. *ACS Omega* **2019,** *4*, 12687-12695.
9. Lv, P.; Lu, Z.; Li, S.; Ma, D.; Zhang, W.; Zhang, Y.; Yang, Z., Tuning metal cluster catalytic activity with morphology and composition: a DFT study of O2 dissociation at the global minimum of PtmPdn (m + n = 5) clusters. *RSC Advances* **2016,** *6*, 104388-104397.
10. Xu, Y.; Shelton, W. A.; Schneider, W. F., Effect of Particle Size on the Oxidizability of Platinum Clusters. *The Journal of Physical Chemistry A* **2006,** *110*, 5839-5846.
11. Kerpal, C.; Harding, D. J.; Hermes, A. C.; Meijer, G.; Mackenzie, S. R.; Fielicke, A., Structures of Platinum Oxide Clusters in the Gas Phase. *The Journal of Physical Chemistry A* **2013,** *117*, 1233-1239.
12. Reber, A. C.; Khanna, S. N.; Roach, P. J.; Woodward, W. H.; Castleman, A. W., Spin Accommodation and Reactivity of Aluminum Based Clusters with O2. *Journal of the American Chemical Society* **2007,** *129*, 16098-16101.
13. Samanta, B.; Sengupta, T.; Pal, S., Aluminum cluster for CO and O2 adsorption. *Journal of Molecular Modeling* **2018,** *25*, 2.

14. Samanta, B.; Sengupta, T.; Pal, S., Specificity of Amino Acid–Aluminum Cluster Interaction and Subsequent Oxygen Activation by the above Complex. *The Journal of Physical Chemistry C* **2018,** *122*, 28310-28323.

15. Burgert, R.; Schnöckel, H.; Grubisic, A.; Li, X.; Stokes, S. T.; Bowen, K. H.; Ganteför, G. F.; Kiran, B.; Jena, P., Spin Conservation Accounts for Aluminum Cluster Anion Reactivity Pattern with O₂. *Science* **2008,** *319*, 438.

16. Neumaier, M.; Olzmann, M.; Kiran, B.; Bowen, K. H.; Eichhorn, B.; Stokes, S. T.; Buonaugurio, A.; Burgert, R.; Schnöckel, H., The Reaction Rates of O2 with Closed-Shell and Open-Shell Alx– and Gax– Clusters under Single-Collision Conditions: Experimental and Theoretical Investigations toward a Generally Valid Model for the Hindered Reactions of O2 with Metal Atom Clusters. *Journal of the American Chemical Society* **2014,** *136*, 3607-3616.

17. Hagen, J.; Socaciu, L. D.; Le Roux, J.; Popolan, D.; Bernhardt, T. M.; Wöste, L.; Mitrić, R.; Noack, H.; Bonačić-Koutecký, V., Cooperative Effects in the Activation of Molecular Oxygen by Anionic Silver Clusters. *Journal of the American Chemical Society* **2004,** *126*, 3442-3443.

18. Socaciu, L. D.; Hagen, J.; Le Roux, J.; Popolan, D.; Bernhardt, T. M.; Wöste, L.; Vajda, Š., Strongly cluster size dependent reaction behavior of CO with O2 on free silver cluster anions. *The Journal of Chemical Physics* **2004,** *120*, 2078-2081.

19. Bernhardt, T. M.; Hagen, J.; Lang, S. M.; Popolan, D. M.; Socaciu-Siebert, L. D.; Wöste, L., Binding Energies of O2 and CO to Small Gold, Silver, and Binary Silver−Gold Cluster Anions from Temperature Dependent Reaction Kinetics Measurements. *The Journal of Physical Chemistry A* **2009,** *113*, 2724-2733.

20. Luo, Z.; Gamboa, G. U.; Smith, J. C.; Reber, A. C.; Reveles, J. U.; Khanna, S. N.; Castleman, A. W., Spin Accommodation and Reactivity of Silver Clusters with Oxygen: The Enhanced Stability of Ag13–. *Journal of the American Chemical Society* **2012,** *134*, 18973-18978.

21. Ma, L.; Melander, M.; Laasonen, K.; Akola, J., CO oxidation catalyzed by neutral and anionic Cu20 clusters: relationship between charge and activity. *Physical Chemistry Chemical Physics* **2015,** *17*, 7067-7076.

22. Haruta, M.; Tsubota, S.; Kobayashi, T.; Kageyama, H.; Genet, M. J.; Delmon, B., Low-Temperature Oxidation of CO over Gold Supported on TiO2, α-Fe2O3, and Co3O4. *Journal of Catalysis* **1993,** *144*, 175-192.

23. Buratto, S. K.; Bowers, M. T.; Metiu, H.; Manard, M.; Tong, X.; Benz, L.; Kemper, P.; Chrétien, S., Chapter 4 Aun and Agn (n=1–8) nanocluster catalysts: gas-phase reactivity to deposited structures. In *The Chemical Physics of Solid Surfaces*, Woodruff, D. P., Ed. Elsevier2007; Vol. 12, pp 151-199.

24. Li, H.; Li, L.; Pedersen, A.; Gao, Y.; Khetrapal, N.; Jónsson, H.; Zeng, X. C., Magic-Number Gold Nanoclusters with Diameters from 1 to 3.5 nm: Relative Stability and Catalytic Activity for CO Oxidation. *Nano Letters* **2015,** *15*, 682-688.

25. Cox, D. M.; Brickman, R.; Creegan, K.; Kaldor, A., Gold clusters: reactions and deuterium uptake. *Zeitschrift für Physik D Atoms, Molecules and Clusters* **1991,** *19*, 353-355.

26. Cox, D. M.; Brickman, R. O.; Creegan, K.; Kaldor, A., Studies of the Chemical Properties of Size Selected Metal Clusters: Kinetics and Saturation. *MRS Proceedings* **2011,** *206*, 43.

27. Salisbury, B. E.; Wallace, W. T.; Whetten, R. L., Low-temperature activation of molecular oxygen by gold clusters: a stoichiometric process correlated to electron affinity. *Chemical Physics* **2000,** *262*, 131-141.

28. Stolcic, D.; Fischer, M.; Ganteför, G.; Kim, Y. D.; Sun, Q.; Jena, P., Direct Observation of Key Reaction Intermediates on Gold Clusters. *Journal of the American Chemical Society* **2003,** *125*, 2848-2849.

29. Kim, Y. D.; Fischer, M.; Ganteför, G., Origin of unusual catalytic activities of Au-based catalysts. *Chemical Physics Letters* **2003,** *377*, 170-176.

30. Huang, W.; Zhai, H.-J.; Wang, L.-S., Probing the Interactions of O2 with Small Gold Cluster Anions (Aun−, n = 1−7): Chemisorption vs Physisorption. *Journal of the American Chemical Society* **2010,** *132*, 4344-4351.
31. Bulusu, S.; Li, X.; Wang, L.-S.; Zeng, X. C., Evidence of hollow golden cages. *Proceedings of the National Academy of Sciences* **2006,** *103*, 8326.
32. Huang, W.; Wang, L.-S., Au10−: isomerism and structure-dependent O2 reactivity. *Physical Chemistry Chemical Physics* **2009,** *11*, 2663-2667.
33. Woodham, A. P.; Meijer, G.; Fielicke, A., Activation of Molecular Oxygen by Anionic Gold Clusters. *Angewandte Chemie International Edition* **2012,** *51*, 4444-4447.
34. Pal, R.; Wang, L.-M.; Pei, Y.; Wang, L.-S.; Zeng, X. C., Unraveling the Mechanisms of O2 Activation by Size-Selected Gold Clusters: Transition from Superoxo to Peroxo Chemisorption. *Journal of the American Chemical Society* **2012,** *134*, 9438-9445.
35. Zhao, Y.; Khetrapal, N. S.; Li, H.; Gao, Y.; Zeng, X. C., Interaction between O2 and neutral/charged Aun (n=1–3) clusters: A comparative study between density-functional theory and coupled cluster calculations. *Chemical Physics Letters* **2014,** *592*, 127-131.
36. Yoon, B.; Häkkinen, H.; Landman, U., Interaction of O2 with Gold Clusters: Molecular and Dissociative Adsorption. *The Journal of Physical Chemistry A* **2003,** *107*, 4066-4071.
37. Sun, Q.; Jena, P.; Kim, Y. D.; Fischer, M.; Ganteför, G., Interactions of Au cluster anions with oxygen. *The Journal of Chemical Physics* **2004,** *120*, 6510-6515.
38. Varganov, S. A.; Olson, R. M.; Gordon, M. S.; Metiu, H., The interaction of oxygen with small gold clusters. *The Journal of Chemical Physics* **2003,** *119*, 2531-2537.
39. Mills, G.; Gordon, M. S.; Metiu, H., The adsorption of molecular oxygen on neutral and negative Aun clusters (n=2–5). *Chemical Physics Letters* **2002,** *359*, 493-499.
40. Ding, X.; Li, Z.; Yang, J.; Hou, J. G.; Zhu, Q., Adsorption energies of molecular oxygen on Au clusters. *The Journal of Chemical Physics* **2004,** *120*, 9594-9600.
41. Wang, Y.; Gong, X. G., First-principles study of interaction of cluster Au32 with CO, H2, and O2. *The Journal of Chemical Physics* **2006,** *125*, 124703.
42. Ding, X.; Dai, B.; Yang, J.; Hou, J. G.; Zhu, Q., Assignment of photoelectron spectra of AunO2− (n=2,4,6) clusters. *The Journal of Chemical Physics* **2004,** *121*, 621-623.
43. Boronat, M.; Corma, A., Oxygen activation on gold nanoparticles: separating the influence of particle size, particle shape and support interaction. *Dalton Transactions* **2010,** *39*, 8538-8546.
44. Lyalin, A.; Taketsugu, T., Reactant-Promoted Oxygen Dissociation on Gold Clusters. *The Journal of Physical Chemistry Letters* **2010,** *1*, 1752-1757.
45. Lee, T. H.; Ervin, K. M., Reactions of Copper Group Cluster Anions with Oxygen and Carbon Monoxide. *The Journal of Physical Chemistry* **1994,** *98*, 10023-10031.
46. Bürgel, C.; Reilly, N. M.; Johnson, G. E.; Mitrić, R.; Kimble, M. L.; Castleman, A. W.; Bonačić-Koutecký, V., Influence of Charge State on the Mechanism of CO Oxidation on Gold Clusters. *Journal of the American Chemical Society* **2008,** *130*, 1694-1698.
47. Tang, D.; Hu, C., DFT Insight into CO Oxidation Catalyzed by Gold Nanoclusters: Charge Effect and Multi-State Reactivity. *The Journal of Physical Chemistry Letters* **2011,** *2*, 2972-2977.
48. Yoon, B.; Häkkinen, H.; Landman, U.; Wörz, A. S.; Antonietti, J.-M.; Abbet, S.; Judai, K.; Heiz, U., Charging Effects on Bonding and Catalyzed Oxidation of CO on Au₈ Clusters on MgO. *Science* **2005,** *307*, 403.
49. Torres, M. B.; Fernández, E. M.; Balbás, L. C., Theoretical Study of Oxygen Adsorption on Pure Aun+1+ and Doped MAun+ Cationic Gold Clusters for M = Ti, Fe and n = 3−7. *The Journal of Physical Chemistry A* **2008,** *112*, 6678-6689.

50. Fernández, E. M.; Torres, M. B.; Balbás, L. C., Theoretical study of the coadsorption of CO and O2 on doped cationic gold clusters MAun+ (M = Ti, Fe, Au; n = 1, 6, 7). *The European Physical Journal D* **2009,** *52*, 135-138.
51. Manzoor, D.; Krishnamurty, S.; Pal, S., Contriving a Catalytically Active Structure from an Inert Conformation: A Density Functional Investigation of Al, Hf, and Ge Doping of Au20 Tetrahedral Clusters. *The Journal of Physical Chemistry C* **2016,** *120*, 19636-19641.
52. Molina, L. M.; Hammer, B., Active Role of Oxide Support during CO Oxidation at $\mathrm{A}\mathrm{u}/\mathrm{M}\mathrm{g}\mathrm{O}$. *Physical Review Letters* **2003,** *90*, 206102.
53. Manzoor, D.; Pal, S., Hydrogen Atom Chemisorbed Gold Clusters as Highly Active Catalysts for Oxygen Activation and CO Oxidation. *The Journal of Physical Chemistry C* **2014,** *118*, 30057-30062.
54. Zhang, C.; Yoon, B.; Landman, U., Predicted Oxidation of CO Catalyzed by Au Nanoclusters on a Thin Defect-Free MgO Film Supported on a Mo(100) Surface. *Journal of the American Chemical Society* **2007,** *129*, 2228-2229.
55. Harding, C.; Habibpour, V.; Kunz, S.; Farnbacher, A. N.-S.; Heiz, U.; Yoon, B.; Landman, U., Control and Manipulation of Gold Nanocatalysis: Effects of Metal Oxide Support Thickness and Composition. *Journal of the American Chemical Society* **2009,** *131*, 538-548.
56. Baishya, S.; Deka, R. C., Hybrid density functional/molecular mechanics studies on activated adsorption of oxygen on zeolite supported gold monomer. *The Journal of Chemical Physics* **2011,** *135*, 244703.
57. Khetrapal, N. S.; Bulusu, S. S.; Zeng, X. C., Structural Evolution of Gold Clusters Aun– (n = 21–25) Revisited. *The Journal of Physical Chemistry A* **2017,** *121*, 2466-2474.
58. Bulusu, S.; Li, X.; Wang, L.-S.; Zeng, X. C., Structural Transitions from Pyramidal to Fused Planar to Tubular to Core/Shell Compact in Gold Clusters: Aun- (n = 21−25). *The Journal of Physical Chemistry C* **2007,** *111*, 4190-4198.
59. Schaefer, B.; Pal, R.; Khetrapal, N. S.; Amsler, M.; Sadeghi, A.; Blum, V.; Zeng, X. C.; Goedecker, S.; Wang, L.-S., Isomerism and Structural Fluxionality in the Au26 and Au26– Nanoclusters. *ACS Nano* **2014,** *8*, 7413-7422.
60. Wang, L.-M.; Wang, L.-S., Probing the electronic properties and structural evolution of anionic gold clusters in the gas phase. *Nanoscale* **2012,** *4*, 4038-4053.
61. Wang, L. S.; Cheng, H. S.; Fan, J., Photoelectron spectroscopy of size-selected transition metal clusters: Fe−n, n=3–24. *The Journal of Chemical Physics* **1995,** *102*, 9480-9493.
62. Wang, L.-S., Photoelectron spectroscopy of size-selected boron clusters: from planar structures to borophenes and borospherenes. *International Reviews in Physical Chemistry* **2016,** *35*, 69-142.
63. Wales, D. J.; Scheraga, H. A., Global Optimization of Clusters, Crystals, and Biomolecules. *Science* **1999,** *285*, 1368.
64. Yoo, S.; Zeng, X. C., Global geometry optimization of silicon clusters described by three empirical potentials. *The Journal of Chemical Physics* **2003,** *119*, 1442-1450.
65. Perdew, J. P.; Burke, K.; Ernzerhof, M., Generalized Gradient Approximation Made Simple. *Physical Review Letters* **1996,** *77*, 3865-3868.
66. Delley, B., From molecules to solids with the DMol3 approach. *The Journal of Chemical Physics* **2000,** *113*, 7756-7764.
67. Delley, B., An all-electron numerical method for solving the local density functional for polyatomic molecules. *The Journal of Chemical Physics* **1990,** *92*, 508-517.
68. Ernzerhof, M.; Scuseria, G. E., Assessment of the Perdew–Burke–Ernzerhof exchange-correlation functional. *The Journal of Chemical Physics* **1999,** *110*, 5029-5036.

69. Ross, R. B.; Powers, J. M.; Atashroo, T.; Ermler, W. C.; LaJohn, L. A.; Christiansen, P. A., Ab initio relativistic effective potentials with spin–orbit operators. IV. Cs through Rn. *The Journal of Chemical Physics* **1990,** *93*, 6654-6670.
70. Frisch, M. J.; Trucks, G. W.; Schlegel, H. B.; Scuseria, G. E.; Robb, M. A.; Cheeseman, J. R.; Scalmani, G.; Barone, V.; Petersson, G. A.; Nakatsuji, H.; Li, X.; Caricato, M.; Marenich, A. V.; Bloino, J.; Janesko, B. G.; Gomperts, R.; Mennucci, B.; Hratchian, H. P.; Ortiz, J. V.; Izmaylov, A. F.; Sonnenberg, J. L.; Williams; Ding, F.; Lipparini, F.; Egidi, F.; Goings, J.; Peng, B.; Petrone, A.; Henderson, T.; Ranasinghe, D.; Zakrzewski, V. G.; Gao, J.; Rega, N.; Zheng, G.; Liang, W.; Hada, M.; Ehara, M.; Toyota, K.; Fukuda, R.; Hasegawa, J.; Ishida, M.; Nakajima, T.; Honda, Y.; Kitao, O.; Nakai, H.; Vreven, T.; Throssell, K.; Montgomery Jr., J. A.; Peralta, J. E.; Ogliaro, F.; Bearpark, M. J.; Heyd, J. J.; Brothers, E. N.; Kudin, K. N.; Staroverov, V. N.; Keith, T. A.; Kobayashi, R.; Normand, J.; Raghavachari, K.; Rendell, A. P.; Burant, J. C.; Iyengar, S. S.; Tomasi, J.; Cossi, M.; Millam, J. M.; Klene, M.; Adamo, C.; Cammi, R.; Ochterski, J. W.; Martin, R. L.; Morokuma, K.; Farkas, O.; Foresman, J. B.; Fox, D. J. *Gaussian 16 Rev. C.01*: Wallingford, CT, 2016.
71. Van Lenthe, E.; Baerends, E. J., Optimized Slater-type basis sets for the elements 1–118. *Journal of Computational Chemistry* **2003,** *24*, 1142-1156.
72. te Velde, G.; Bickelhaupt, F. M.; Baerends, E. J.; Fonseca Guerra, C.; van Gisbergen, S. J. A.; Snijders, J. G.; Ziegler, T., Chemistry with ADF. *Journal of Computational Chemistry* **2001,** *22*, 931-967.
73. *ADF 2019.3, SCM, Theoretical Chemistry*: Vrije Universiteit, Amsterdam, The Netherlands, 2019.
74. Valiev, M.; Bylaska, E. J.; Govind, N.; Kowalski, K.; Straatsma, T. P.; Van Dam, H. J. J.; Wang, D.; Nieplocha, J.; Apra, E.; Windus, T. L.; de Jong, W. A., NWChem: A comprehensive and scalable open-source solution for large scale molecular simulations. *Computer Physics Communications* **2010,** *181*, 1477-1489.
75. Khetrapal, N. S.; Jian, T.; Lopez, G. V.; Pande, S.; Wang, L.-S.; Zeng, X. C., Probing the Structural Evolution of Gold–Aluminum Bimetallic Clusters (Au2Aln–, n = 3–11) Using Photoelectron Spectroscopy and Theoretical Calculations. *The Journal of Physical Chemistry C* **2017,** *121*, 18234-18243.
76. Khetrapal, N. S.; Jian, T.; Pal, R.; Lopez, G. V.; Pande, S.; Wang, L.-S.; Zeng, X. C., Probing the structures of gold–aluminum alloy clusters AuxAly−: a joint experimental and theoretical study. *Nanoscale* **2016,** *8*, 9805-9814.
77. Khetrapal, N. S.; Wang, L.-S.; Zeng, X. C., Determination of CO Adsorption Sites on Gold Clusters Aun– (n = 21–25): A Size Region That Bridges the Pyramidal and Core–Shell Structures. *The Journal of Physical Chemistry Letters* **2018,** *9*, 5430-5439.
78. Shao, N.; Huang, W.; Gao, Y.; Wang, L.-M.; Li, X.; Wang, L.-S.; Zeng, X. C., Probing the Structural Evolution of Medium-Sized Gold Clusters: Aun− (n = 27−35). *Journal of the American Chemical Society* **2010,** *132*, 6596-6605.
79. Pande, S.; Jian, T.; Khetrapal, N. S.; Wang, L.-S.; Zeng, X. C., Structural Evolution of Gold-Doped Bismuth Clusters AuBin– (n = 4–8). *The Journal of Physical Chemistry C* **2018,** *122*, 6947-6954.
80. Li, J.; Li, X.; Zhai, H.-J.; Wang, L.-S., Au₂₀: A Tetrahedral Cluster. *Science* **2003,** *299*, 864.
81. Gu, X.; Bulusu, S.; Li, X.; Zeng, X. C.; Li, J.; Gong, X. G.; Wang, L.-S., Au_{34}^{-}: A Fluxional Core−Shell Cluster. *The Journal of Physical Chemistry C* **2007,** *111*, 8228-8232.
82. Henkelman, G.; Arnaldsson, A.; Jónsson, H., A fast and robust algorithm for Bader decomposition of charge density. *Computational Materials Science* **2006,** *36*, 354-360.
83. Sanville, E.; Kenny, S. D.; Smith, R.; Henkelman, G., Improved grid-based algorithm for Bader charge allocation. *Journal of Computational Chemistry* **2007,** *28*, 899-908.
84. Tang, W.; Sanville, E.; Henkelman, G., A grid-based Bader analysis algorithm without lattice bias. *Journal of Physics: Condensed Matter* **2009,** *21*, 084204.

Appendix

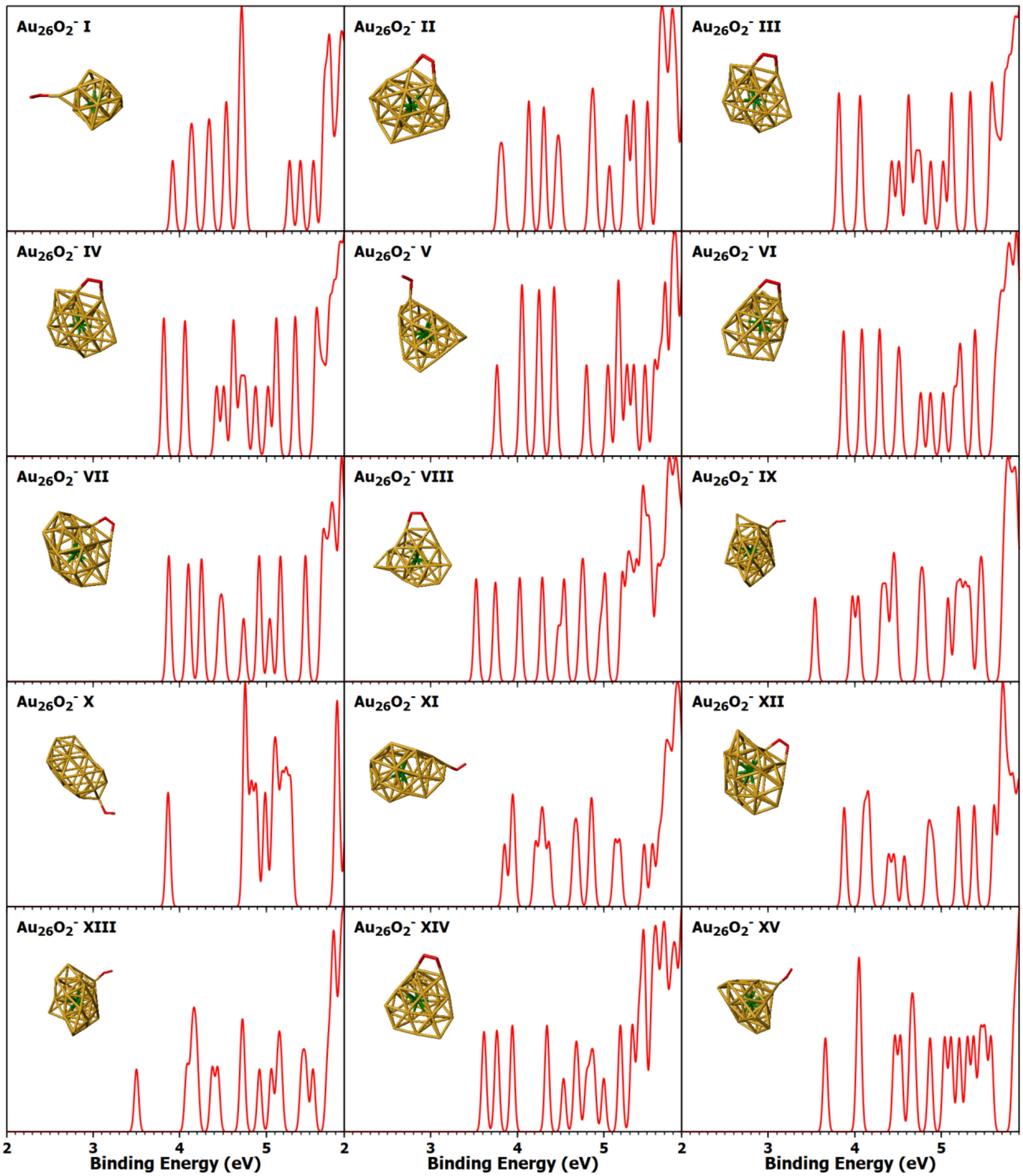

Figure 7. Simulated spectra of the low-lying isomers of $Au_{26}O_2^-$. The gold atoms in green denote the atoms in the core of the cluster. The oxygen molecule is in red.

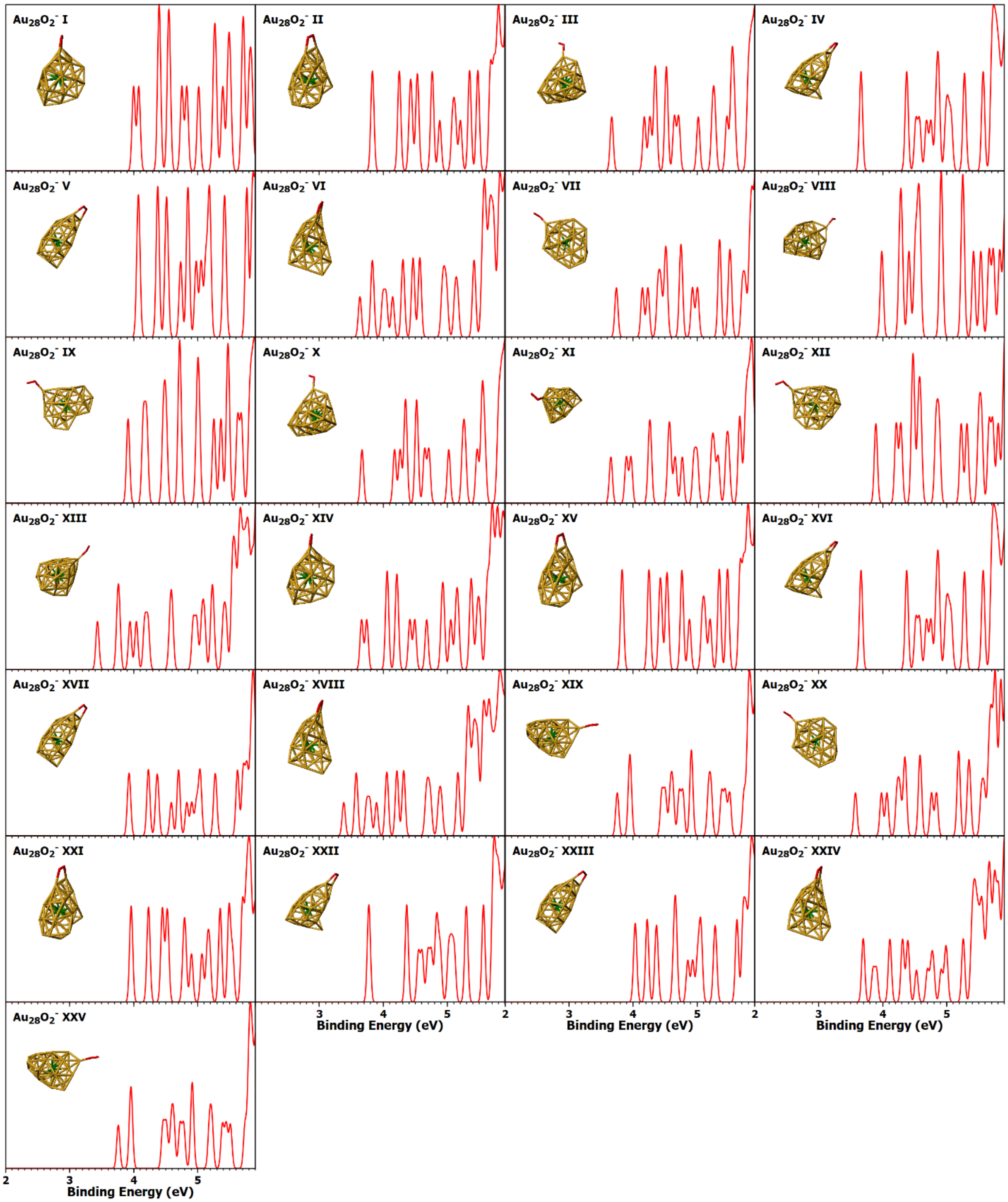

Figure 8. Simulated spectra of the low-lying isomers of $Au_{28}O_2^-$. The gold atoms in green denote the atoms in the core of the cluster. The oxygen molecule is in red.

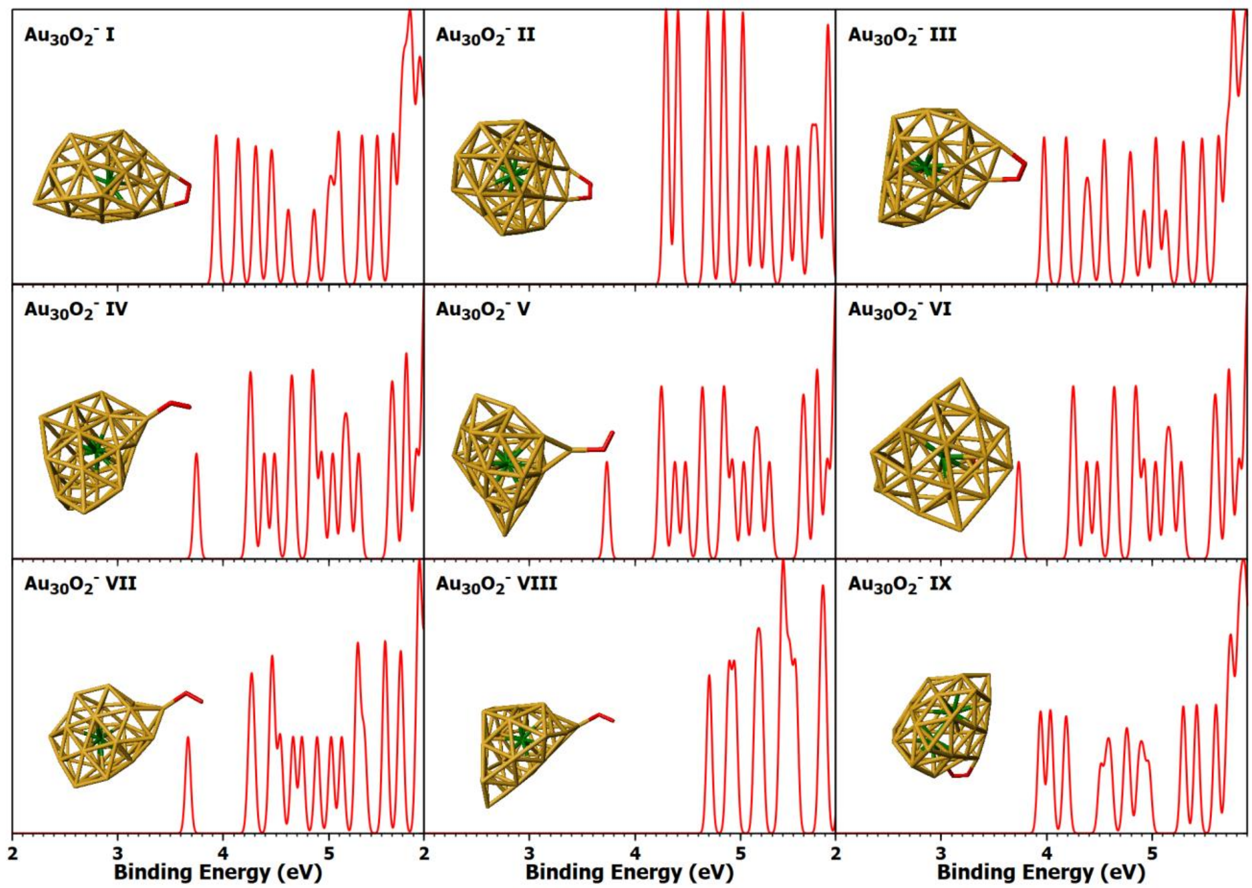

Figure 9. Simulated spectra of the low-lying isomers of $Au_{30}O_2^-$. The gold atoms in green denote the atoms in the core of the cluster. The oxygen molecule is in red.

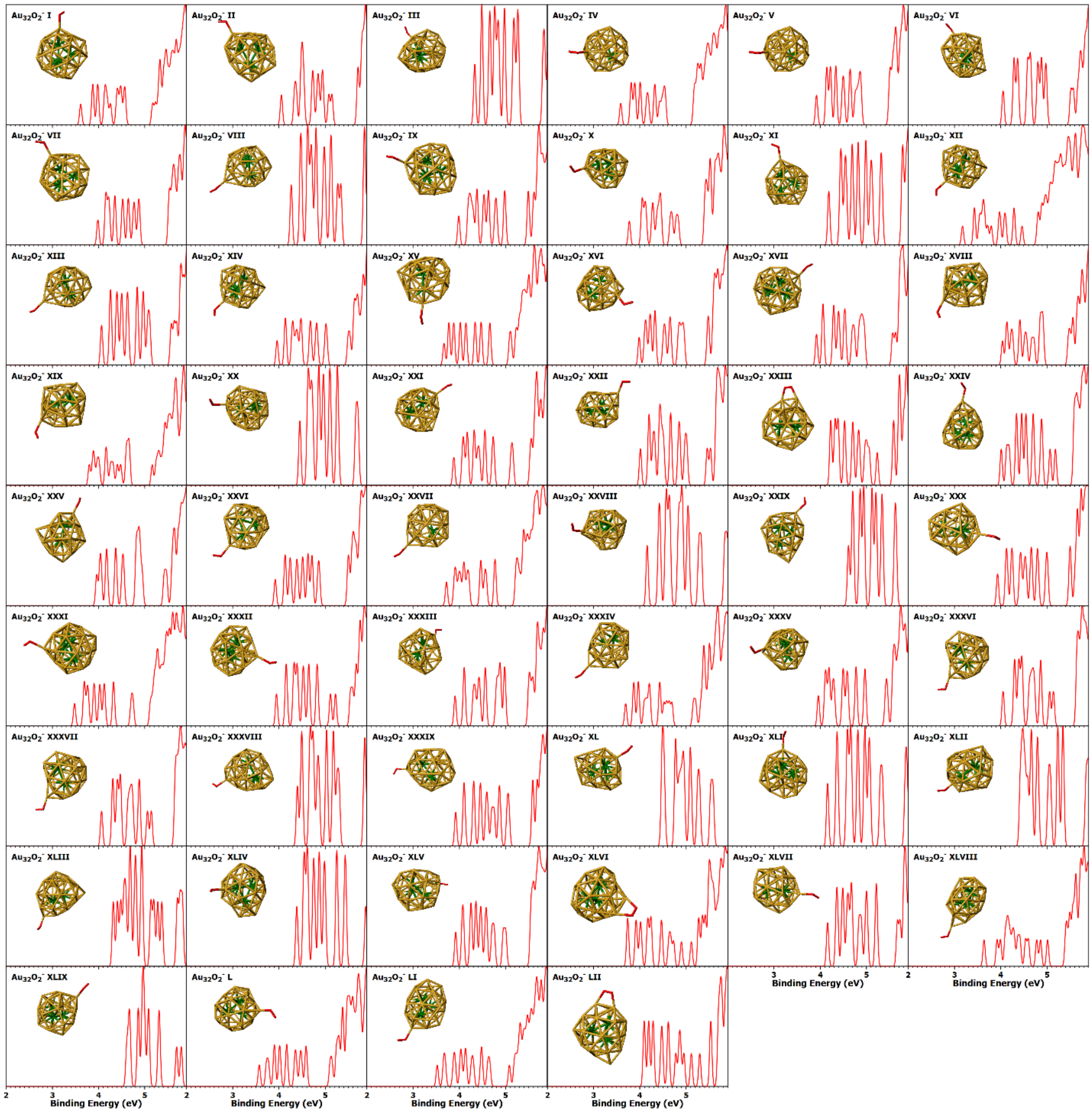

Figure 10. Simulated spectra of the low-lying isomers of $Au_{32}O_2^-$. The gold atoms in green denote the atoms in the core of the cluster. The oxygen molecule is in red.

Table 2. Relative energies of $Au_{26}O_2^-$ simulated isomers. Relative energies computed at PBE0/TZP with inclusion of relativistic ZORA effects (ΔE_a) and PBE0/CRENBL-EXCP (including SO effects for Au) (ΔE_b) The theoretical VDE and energy gap between X-A peak positions. All values are in eV.

Isomer	**ΔE_a**	**ΔE_b**	**VDE**	**Gap**
I	0.000	0.319	3.920	0.236
II	0.350	0.161	3.793	0.339
III	0.893	0.001	3.813	0.242
IV	0.895	0.000	3.813	0.242
V	1.903	0.324	3.767	0.297
VI	1.906	0.086	3.866	0.215
VII	2.335	0.151	3.873	0.219
VIII	2.721	0.539	3.521	0.219
IX	3.286	0.304	3.541	0.499
X	3.913	0.580	3.866	0.895
XI	4.776	0.545	3.853	0.106
XII	5.425	0.276	3.873	0.223
XIII	5.909	0.387	3.501	0.639
XIV	6.044	0.556	3.607	0.150
XV	7.689	0.510	3.661	0.397

Table 3. Relative energies of $Au_{28}O_2^-$ simulated isomers. Relative energies computed at PBE0/TZP with inclusion of relativistic ZORA effects (ΔE_a) and PBE0/CRENBL-EXCP (including SO effects for Au) (ΔE_b) The theoretical VDE and energy gap between X-A peak positions. All values are in eV.

Isomer	ΔE_a	ΔE_b	VDE	Gap
I	0.000	0.054	3.694	0.155
II	0.171	0.447	3.634	0.203
III	0.672	0.151	4.066	0.309
IV	0.767	0.000	4.026	0.193
V	2.010	0.424	3.740	0.492
VI	3.003	0.189	3.654	0.313
VII	3.410	0.364	3.960	0.268
VIII	3.795	0.158	3.661	0.713
IX	4.164	0.093	3.773	0.591
X	4.855	0.206	3.986	0.310
XI	4.865	0.190	3.999	0.395
XII	6.580	0.121	3.827	0.419
XIII	6.624	0.283	3.913	0.289
XIV	7.293	0.256	3.893	0.390
XV	7.683	0.281	3.667	0.595
XVI	7.683	0.281	3.667	0.596
XVII	8.667	0.425	3.754	0.206
XVIII	8.668	0.425	3.760	0.205
XIX	8.914	0.424	3.574	0.492
XX	9.985	0.301	3.435	0.339
XXI	10.932	0.158	3.661	0.713
XXII	11.816	0.121	3.827	0.419
XXIII	12.213	0.447	3.382	0.203
XXIV	12.728	0.190	3.661	0.395
XXV	14.771	0.151	3.920	0.309

Table 4. Relative energies of $Au_{30}O_2^-$ simulated isomers. Relative energies computed at PBE0/TZP with inclusion of relativistic ZORA effects (ΔE_a) and PBE0/CRENBL-EXCP (including SO effects for Au) (ΔE_b) The theoretical VDE and energy gap between X-A peak positions. All values are in eV.

Isomer	ΔE_a	ΔE_b	VDE	Gap
I	0.000	0.000	3.933	0.003
II	3.385	0.085	4.292	0.005
III	4.155	0.064	3.973	0.004
IV	5.518	0.284	3.747	0.500
V	5.536	0.280	3.734	0.505
VI	5.537	0.280	3.734	0.505
VII	5.908	0.342	3.667	0.587
VIII	6.086	0.391	4.704	0.185
IX	6.579	0.149	3.933	0.016
X	6.579	0.149	4.876	0.016
XI	6.954	0.147	3.933	0.017

Table 5. Relative energies of $Au_{32}O_2^-$ simulated isomers. Relative energies computed at PBE0/TZP with inclusion of relativistic ZORA effects (ΔE_a) and PBE0/CRENBL-EXCP (including SO effects for Au) (ΔE_b) The theoretical VDE and energy gap between X-A peak positions. All values are in eV.

Isomer	ΔE_a	ΔE_b	VDE	Gap
I	0.000	0.322	3.614	0.257
II	0.300	0.540	4.053	0.424
III	3.741	0.142	4.332	0.317
IV	4.103	0.484	3.587	0.298
V	4.278	0.164	3.920	0.295
VI	4.814	0.250	4.053	0.233
VII	5.658	0.224	3.986	0.225
VIII	5.948	0.190	4.265	0.199
IX	5.956	0.243	3.986	0.201
X	6.229	0.636	3.773	0.336
XI	6.724	0.538	4.185	0.346
XII	6.744	1.084	3.176	0.253
XIII	6.979	0.477	4.066	0.322
XIV	7.261	0.229	3.960	0.172
XV	7.548	1.253	3.667	0.101
XVI	7.714	0.304	3.986	0.122
XVII	7.767	0.210	3.920	0.135
XVIII	7.879	0.374	4.039	0.084
XIX	7.951	0.626	3.800	0.074
XX	7.961	0.039	4.451	0.241
XXI	8.087	0.041	3.880	0.283
XXII	8.220	0.295	4.013	0.181
XXIII	8.274	0.000	4.225	0.006
XXIV	8.338	0.318	4.013	0.116
XXV	8.447	0.285	3.960	0.068
XXVI	8.861	0.247	3.920	0.313
XXVII	8.874	0.602	3.720	0.264
XXVIII	9.204	0.189	4.159	0.249
XXIX	9.205	0.627	4.611	0.245
XXX	9.558	0.336	3.933	0.183
XXXI	9.859	0.499	3.481	0.205
XXXII	10.154	0.266	3.946	0.205
XXXIII	10.341	0.437	3.906	0.193
XXXIV	10.488	0.601	3.694	0.171
XXXV	10.698	0.263	3.960	0.145
XXXVI	10.938	0.473	4.053	0.242
XXXVII	11.183	0.480	4.066	0.236
XXXVIII	11.286	0.387	4.398	0.266
XXXIX	11.831	0.404	3.920	0.173
XL	12.577	0.440	4.478	0.020
XLI	13.042	0.305	4.159	0.419
XLII	13.519	0.442	4.425	0.040
XLIII	14.112	0.731	4.318	0.089
XLIV	15.024	0.592	4.385	0.149
XLV	15.130	0.421	3.920	0.322
XLVI	15.137	0.383	3.734	0.009
XLVII	15.678	0.746	4.159	0.191
XLVIII	16.031	0.677	3.641	0.282
XLIX	17.328	0.387	4.611	0.048
L	18.168	0.965	3.574	0.321
LI	18.518	0.851	3.521	0.138
LII	18.977	0.475	4.092	0.005